



Optimization of material removal rate in milling of thin-walled structures using penalty cost function

Kasper Ringgaard^{a,*}, Yaser Mohammadi^b, Christian Merrild^c, Ole Balling^a, Keivan Ahmadi^b

^a Section of Mechanical Engineering, Department of Engineering, Aarhus University, DK-8000, Aarhus, Denmark

^b Department of Mechanical Engineering, University of Victoria, Victoria, British Columbia, V8W 2Y2, Canada

^c Danish Advanced Manufacturing Research Center, DK-7400, Herning, Denmark

ARTICLE INFO

Keywords:

Milling
Optimization
Finite strip modelling
Flexible workpiece
Chatter
Forced vibrations

ABSTRACT

The high flexibility of thin-walled structures makes their machining process prone to chatter and excessive vibrations. This challenge is compounded by the continuous varying dynamics of the workpiece as material is removed from the workpiece. As a result, the common optimization methods that are used for maximizing material removal rate in the milling processes of rigid parts are not applicable to machining of thin-walled structures. In this paper, an optimization method is presented to maximize the material removal rate in milling of thin-walled structures without violating forced vibration and chatter stability constraints. The cost function of the optimization problem is formulated using penalty terms to impose the vibration constraints. Moreover, a resampling strategy is implemented to minimize the risk of convergence to a local minimum. The performance of the presented approach is studied through planning of the semi-finishing stage of machining a thin-walled pocket structure. The dynamics of the workpiece is modelled using finite strip modelling to ensure high computational efficiency. The numerical simulations and experimental studies in this work show that the presented optimization approach can be effectively used to plan an optimum machining process for thin-walled structures which does not cause chatter or excessive vibration amplitudes.

1. Introduction

Thin-walled pocket components are widely used in the fuselages and wing structures of aircrafts. Pocket structures are typically manufactured using milling processes where large amounts of material is machined from a solid block. It is key to perform the machining operations as fast as possible to lower production cost. Vibrations are present when performing semi-finishing and finishing operations, where the pocket wall rigidity is low. Large vibrations levels or unstable vibrations yields parts with poor surface quality and in severe cases the parts have to be scrapped. The current industry practice to increase the Material Removal Rate (MRR) is mainly based on the application of craftsman-knowledge and expensive trial and error tests.

In recent decades various approaches aiming at replacing trial and errors with process modelling and computer simulations have been published. Examples are: Rai et al. [1] who used finite element models for milling process plan verification including both thermal- and mechanical loads; Chen et al. [2] used finite element analysis for prediction of deflections in multilayer milling for thin-walled parts; Zhang et al. [3] introduced *synthetical stability lobes* which accounts for both

Surface Location Error (SLE) and chatter limits using experimental or simulation results. The general idea in literature is to develop predictive models of the manufacturing process and use them for simulation of the process instead of performing physical trials on a machine tool. This approach allows selection of proper process parameters (e.g. spindle speed and depth of cut) without using costly machine time and materials. Employing this approach for the machining of thin-walled structures is challenging, as the dynamics of the workpiece changes continuously when material is removed. Hence, the simulation of the process requires regular updating of the dynamic model representing the workpiece. Determining the optimum cutting conditions requires repeating the simulation for various combinations of process parameters such as feed rate, spindle speed, and depth of cut, which renders a significant computational burden. Bolsunovskiy et al. [4] is an example of the complexity of this task: First they created and meshed finite element geometries for a blade at six different stages during the machining process, second they ran modal analysis to obtain modal parameters and third they compared a set of structural frequencies to the cutting force harmonics to manually determine appropriate spindle speeds (i.e. only one process parameter). To overcome these limits it is

* Corresponding author.

E-mail address: kri@eng.au.dk (K. Ringgaard).

<https://doi.org/10.1016/j.ijmactools.2019.103430>

Received 1 March 2019; Received in revised form 27 May 2019; Accepted 4 July 2019

Available online 09 July 2019

0890-6955/ © 2019 Elsevier Ltd. All rights reserved.

essential to a) develop computationally efficient methods to model the varying dynamics of the flexible workpiece, and b) to use efficient optimization algorithms to reduce the number of simulations required to determine the optimum cutting parameters.

Finite element models have been applied by multiple researchers, e.g. Refs. [5–7], to model the dynamics of the flexible workpiece during machining, but the common problem with application of the finite element method is to efficiently update the mesh of the model to mimic the material that is continuously removed. Bauman et al. [8] proposed to limit the computation time through parametric model order reduction. Recent research by Tuysuz [9] demonstrated that perturbation methods yield an even faster way to obtain the workpiece structural model in different stages of the process. In a similar way Yang et al. [10] proposed a method where the workpiece is decomposed into machined workpiece and material to be removed and coupled them using component mode synthesis. This method removed the need for recomputing the response of a large finite element model for each step throughout the machining process. An alternative approach was recently suggested by Wang et al. [11]. They proposed accounting for changes caused by material removal by perturbation of the unmachined workpiece matrices using third order Taylor series for approximation of the system matrix variation with wall thickness for a curved blade structure. While the finite element method combined with some of the methods mentioned is advantageous for the general complex structure, more efficient methods exist for thin-walled plate and shell structures. The semi-analytical method of finite strip modelling has been shown to predict dynamic response of thin-walled structures fast and reliably [12].

A few examples of maximizing MRR using predictive models are found in literature. One example is Budak and Tekeli [13] who optimized the MRR in pocket machining considering only a constraint of a chatter free process. Variation of radial and axial depth of cut are considered, and the spindle speed is kept constant. The dynamic response of the cutting tool is constant throughout the process, and the optimization is based on manual selection based on limit plots. Another example is Zhang and Ding [14] who presented an optimization formulation where the MRR is maximized while the dynamic deflections are minimized. Two design variables are chosen: spindle speed and axial depth of cut. The problem is formulated as a sequential optimization problem of minimizing the deflections while obeying constraints on stability, maximum spindle speed and improving of the MRR compared to previous steps. The modal parameters of the spindle-tool assembly are assumed constant, and the corresponding stability lobe is computed. The problem is solved using the gradient based augmented Lagrangian function method, which yields result that are highly dependent on initial guess.

The aforementioned research covers both modelling of varying workpiece dynamics, increasing the efficiency of the computations and different approaches of selecting optimal cutting parameters through manual selection or using optimization routines. Nonetheless, limited attention has been given to combining all of these methods into one efficient optimization setup which automatically accounts for varying dynamics while determining optimal cutting parameters which obeys constraints related to vibrations. This paper presents a new formulation of an optimization problem capable of incorporating all these effects.

An optimization problem that maximizes the material removal rate in thin-walled machining while complying with constraints on vibration amplitude and process stability (i.e. chatter) and accounting for varying structural dynamics is formulated. The deflection and chatter stability constraints are incorporated in the cost function using the penalty method [15]. Implementing the penalty method instead of computing constraint equations for each iterations yields higher computational efficiency. Computing the non-linear constraint equations of each new set of design variables is time consuming, whereas the penalty method basically just evaluates the penalty value for the current design point. The penalty terms rely on predictive models of chatter stability

and forced vibrations [16]. Instead of evaluating the penalty terms at all of the cutter locations along the toolpath, only a subset of the cutter locations are used to increase the computational speed. These cutter locations are selected using a critical point identification technique proposed in this paper. The proposed optimization algorithm is conducted using a gradient based search approach combined with a history based resampling strategy to increase the likelihood of finding the global minimum. The proposed method is applicable to any model structure which can be updated for discrete steps throughout the process. In this contribution, it is applied to a case study optimizing the semi-finishing stage of machining an aluminium pocket. The pocket is modelled using finite strip modelling as described in Ref. [12]. Using a numerical example it is demonstrated that the penalty based cost function successfully represents the active chatter constraint, and that the deflection constraint is dominant inside some stability pockets. The numerical example is also used to show that the optimization and resampling strategies comply with the active constraints in an acceptable manner. Through milling experiments it is shown that machining process parameters determined by the optimization routine ensures deflections below the specified threshold and that no instability is encountered.

The finite strip modelling used to model the workpiece is briefly introduced in Section 2. Section 3 describes cutting force modelling, the theory behind regenerative chatter prediction and computation of vibration amplitudes. The cost function, critical point identification, resampling strategy and optimization routine are explained in Section 4. Section 5 describes the case study and Section 6 presents a numerical example of the performance of the optimization algorithm. Section 7 describes the experimental validation of the proposed optimization strategy and a conclusion is presented in Section 8.

2. Finite strip modelling

A brief description of the finite strip modelling of varying dynamics of straight thin-walled structures is provided in this section for completeness. A detailed description of the method is available in Ref. [12]. For curved thin-walled structures the finite strip method presented in Ref. [17] can be applied in the proposed optimization method instead. For this contribution, a single pocket with four sides is used for both explanation and case study, see Fig. 1. In the semi-finishing passes the thickness to length ratio is sufficiently small to model the walls using Kirchhoff's thin plate theory [18]. In-plane deflections (membrane) are neglected due to chip thickness and cutting forces mainly being affected by out-of-plane deflections (bending). Each side of the pocket is discretized into a number of equal length strips Δu , defined by their neutral planes. Furthermore, each strip is assumed to consist of two spans in the height direction (v), which can have different thicknesses t_1 and t_2 representing before and after a tool pass respectively. In the actual process, material is machined from one side of the wall only, but in the finite strip modelling the material removal is assumed to be symmetric around the center plane of the strip. The stiffness of the workpiece holder is large compared to the thin walls, and therefore a clamped boundary condition is assumed at the bottom of each strip. Considering these assumptions, the displacement field of one strip in the out-of-plane direction ($w(u,v,t)$) is approximated by a series of trigonometric functions $Y_p(v)$ that satisfy clamped-free boundary conditions, as follows:

$$w(u,v,t) = \sum_{p=1}^m f_p(u, t) Y_p(v) \quad (1)$$

$$Y_p(v) = 1 - \cos\left(p - \frac{v\pi}{2H}\right) \quad (2)$$

where m is the number of trigonometric terms considered in the approximation, and v and u denote vertical and horizontal coordinates, respectively. Combining the trigonometric expansion functions $Y_p(v)$

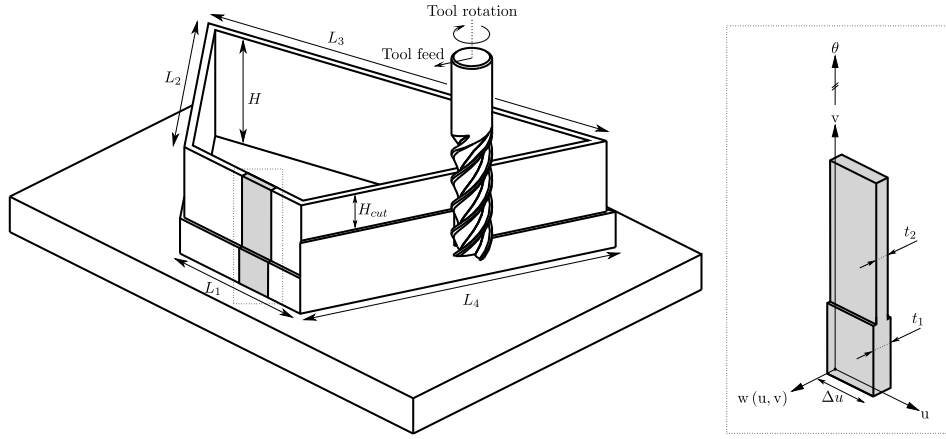


Fig. 1. General four sided pocket structure (left) and single finite strip (right).

with appropriate one dimensional polynomial shape functions $f_p(u, t)$, the problem of determining the two dimensional displacement field $w(u, v, t)$ is transformed into a one dimensional problem. Two degrees of freedom are utilized for each nodal line: w_{1p} and θ_{1p} at $u = 0$ and w_{2p} and θ_{2p} at $u = \Delta u$. Introducing shape functions in Eqn. (1) yields the spatial out-of-plane deflections $(w(u, v, t))$ described using nodal coordinates $\mathbf{d}_p(t) = [w_{1p}(t) \ \theta_{1p}(t) \ w_{2p}(t) \ \theta_{2p}(t)]^T$ as:

$$w(u, v, t) = \sum_{p=1}^m \mathbf{S}_p(u, v) \mathbf{d}_p(t) \quad (3)$$

$$\mathbf{S}_p(u, v) = [S_1(u) \ S_2(u) \ S_3(u) \ S_4(u)] \mathbf{Y}_p(v) \quad (4)$$

with shape functions given as:

$$\begin{aligned} S_1(u) &= (1 - 3\bar{u}^2 + 2\bar{u}^3); \quad S_2(u) = u(1 - 2\bar{u} + \bar{u}^2) \\ S_3(u) &= (3\bar{u}^2 - 2\bar{u}^3); \quad S_4(u) = u(-\bar{u} + \bar{u}^2) \end{aligned} \quad (5)$$

where $\bar{u} = \frac{u}{\Delta u}$. Each corner of the pocket is assumed to be simply supported. This is enforced by eliminating corresponding rows and columns in the mass and stiffness matrices of the structure. Derivation of mass and stiffness matrices, $[\mathbf{M}]$ and $[\mathbf{K}]$, and mathematical descriptions of boundary conditions are explained in Ref. [12].

2.1. Frequency response function

Mass and stiffness matrices resulting from the finite strip model can be diagonalized to obtain the modal mass matrix $[\mathbf{M}_q]$ and modal stiffness matrix $[\mathbf{K}_q]$ as:

$$[\mathbf{M}_q] = [\mathbf{V}]^T [\mathbf{M}] [\mathbf{V}]; \quad [\mathbf{K}_q] = [\mathbf{V}]^T [\mathbf{K}] [\mathbf{V}] \quad (6)$$

where the N_r eigenvectors $[\mathbf{V}] = [\mathbf{v}_1, \mathbf{v}_2, \dots, \mathbf{v}_{N_r}]$ are determined through the eigenvalue problem:

$$([\mathbf{K}] - [\mathbf{M}]\lambda_r) \mathbf{v}_r = 0 \quad (7)$$

with λ_r being the eigenvalue and \mathbf{v}_r being the corresponding eigenvector, for $r = 1 \dots N_r$. Damping of the workpiece structure is not modelled, but modal damping ratios can be obtained through experimental modal analysis on the component being modelled [19]. The modal damping matrix can be obtained by combining the measured modal damping ratios and the modal mass and stiffness matrices as follows:

$$[\mathbf{C}_q] = 2[\mathbf{Z}] \sqrt{[\mathbf{K}_q][\mathbf{M}_q]} \quad (8)$$

where $[\mathbf{Z}]$ is a diagonal matrix of experimentally determined damping ratios (ζ_r).

For the strip of interest the eigenvector of Eqn. (7) at coordinates (u, v) is transformed to a physical deflection mode shape $(w(u, v))$ using the shape functions of Eqns. (3) and (5) as:

$$\varphi_r(u, v) = \sum_{p=1}^m \mathbf{S}_p(u, v) \bar{\mathbf{d}}_p \quad (9)$$

where $\bar{\mathbf{d}}_p$ is nodal coordinates from corresponding eigenvector \mathbf{v}_r for the strip of interest. The continuous mode shapes, $\varphi_r(u, v)$, can be converted into the mode shape vector by evaluating them at a set of discrete points, O_1 to O_{N_0} , located on the strip of interest. The mode shape matrix is obtained by collecting the resulting mode shape vectors in a matrix form as follows:

$$[\Phi] = \begin{bmatrix} \varphi_1(O_1) & \dots & \varphi_{N_r}(O_1) \\ \vdots & \ddots & \vdots \\ \varphi_1(O_{N_0}) & \dots & \varphi_{N_r}(O_{N_0}) \end{bmatrix} \quad (10)$$

The Laplace domain transfer function matrix, containing both direct and cross terms, is obtained through combining the mode shape matrix of Eqn. (10) and the modal matrices of Eqn. (6) and Eqn. (8) as:

$$[\mathbf{G}(s)] = [\Phi]([\mathbf{M}_q]s^2 + [\mathbf{C}_q]s + [\mathbf{K}_q])^{-1}[\Phi]^T \quad (11)$$

where entry l, n of $[\mathbf{G}(s)]$ is the transfer function from point O_l to point O_n . The frequency response function is obtained by converting Eqn. (11) to frequency domain by setting $s = i\omega$.

3. Regenerative and forced vibrations

The maximum achievable material removal rate in thin-walled machining is constrained by surface and tolerance requirements of the workpiece. To obtain a proper surface finish and satisfy dimensional tolerances, it is essential to ensure that workpiece vibrations are stable and their amplitudes are low. A common way of managing the vibrations during thin-walled machining is through selection of proper cutting parameters. In this paper the selection of cutting parameters is based on the dynamic simulation of the cutting process by combining the dynamic model presented in the previous section with a linear mechanistic cutting force model [16]. The resulting model is used for prediction of regenerative chatter instability and forced response amplitudes. The two phenomena are treated separately in this paper. The total axial depth of engagement of the tool, a , is discretized into N_a discs of equal height $\Delta a = \frac{a}{N_a}$, as shown in Fig. 2. The dynamics of the system in the Laplace domain is described by Eqn. (12).

$$\mathbf{w}(s) = [\mathbf{G}(s)] \mathbf{F}(s) \quad (12)$$

The transfer function, $[\mathbf{G}(s)]$, is computed according to Eqn. (11), where mode shapes are computed for center points of the tool discs ($O_1 \dots O_{N_0}$) following Eqn. (10) with $N_0 = N_a$. The transfer function, i.e. the workpiece dynamics, is updated for every step in the machining process such that the response at the cutting tool is representative of the actual workpiece geometry. The frequency response functions are

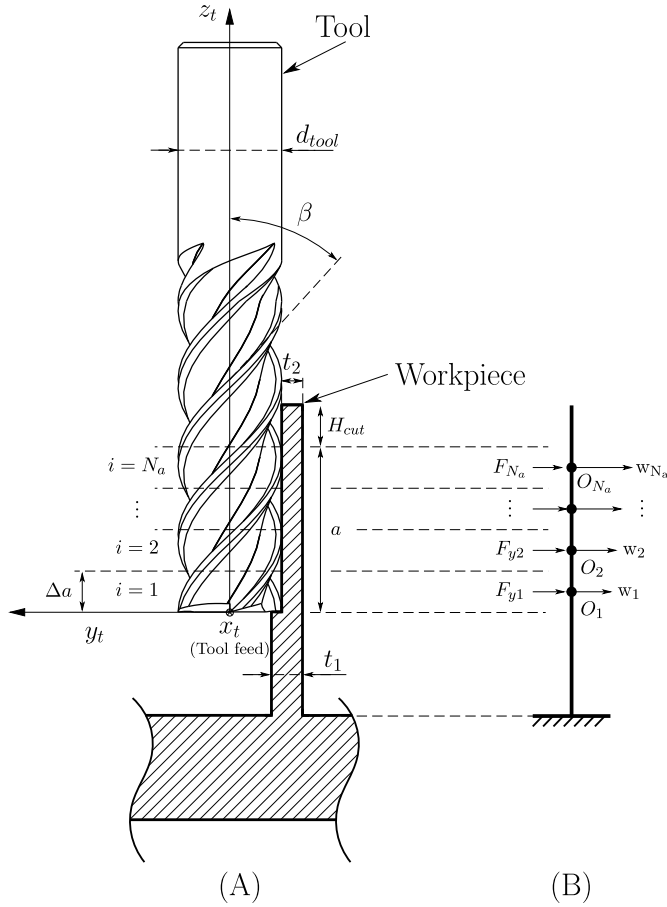


Fig. 2. Axial discretization of cutting tool and pocket wall. (A) detailed sketch (B) discretization sketch.

updated after machining of each strip in each machining pass. In Eqn. (12), $\mathbf{w}(s)$ is the vector of out-of-plane deflections of the pocket wall at O_1 to O_{N_a} , and $\mathbf{F}(s)$ is the vector of corresponding forces normal to the pocket wall at those points. The deflection vector $\mathbf{w}(s)$ and the force vector $\mathbf{F}(s)$ are given by:

$$\begin{aligned} \mathbf{w}(s) &= [w_1(s) \ w_2(s) \ \cdots \ w_{N_a}(s)]^T \\ \mathbf{F}(s) &= [F_{y1}(s) \ F_{y2}(s) \ \cdots \ F_{yN_a}(s)]^T \end{aligned} \quad (13)$$

The normal cutting forces applied on each disc are computed according to Sec. 3.1, and they are assumed to be concentrated at the center points of the tool discs.

3.1. Cutting force model

Machining forces are described using the linear mechanistic force model [16]. Axial forces are neglected due to the relatively high wall stiffness in that direction. At the location of each axial element, $i = 1 \dots N_a$, tangential (F_t) and radial (F_r) cutting forces are exerted on the workpiece by each flute of the cutting tool ($j = 1 \dots N_f$), as illustrated in Fig. 3. The force model is described as follows:

$$\begin{bmatrix} F_{tji}(t) \\ F_{rji}(t) \end{bmatrix} = \Delta a \begin{bmatrix} K_{tc} \\ K_{rc} \end{bmatrix} h(\phi_{ji}(t)) + \begin{bmatrix} K_{te} \\ K_{re} \end{bmatrix} \quad (14)$$

where K_{tc} and K_{rc} are the cutting force coefficients and K_{te} and K_{re} are the edge force coefficients. $\phi_{ji}(t)$ is the angular position of the j^{th} flute on the i^{th} axial disc, which is described by

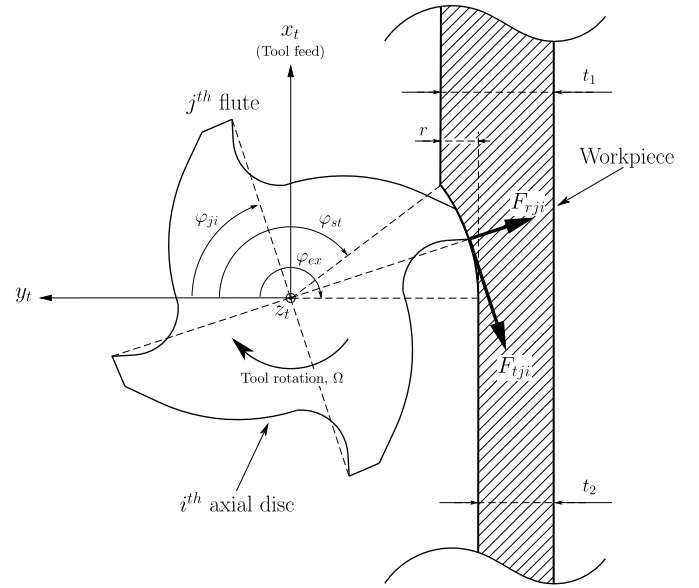


Fig. 3. Cutting tool section with forces.

$$\phi_{ji}(t) = \Omega t - (j - 1) \frac{2\pi}{N_f} - i \Delta a \frac{2 \tan(\beta)}{d_{tool}} \quad (15)$$

where Ω is the spindle speed, N_f is the number of flutes, β is the helix angle and d_{tool} is the tool diameter (see Fig. 2). The chip thickness $h(\phi_{ji}(t))$ is described as:

$$\begin{aligned} h(\phi_{ji}(t)) &= h_{st} - h_{dyn} \\ &= s_t \sin \phi_{ji}(t) - \Delta w_i(t) \cos \phi_{ji}(t) \Delta w_i(t) \\ &= w_i(t) - w_i(t - T) \end{aligned} \quad (16)$$

where h_{st} and h_{dyn} are the static and dynamic chip thickness respectively, and the tooth passing period T is given by:

$$T = \frac{1}{\Omega N_f} \quad (17)$$

The first term of Eqn. (16) (h_{st}) is the static chip thickness generated by the feed motion of the tool, s_t . The static part of the chip thickness generates harmonic forces at the tooth passing frequency, which in turn excites forced vibrations of the pocket wall. The second term (h_{dyn}) is the regenerative chip thickness, which is generated by vibrations of the workpiece in the current time step $w_i(t)$ and vibration marks left by the previous flute at the same location $w_i(t - T)$. A more detailed description of the composition of regenerative chip thickness is provided in Sec. 3.2. The regenerative part of the chip thickness results in self-excited vibrations which can become unstable and lead to chatter. Index i is the axial element of interest on the tool and therefore $w_i(t)$ can be evaluated for the corresponding point on the pocket using proper coordinates u, v in Eqn. (3).

The normal force applied to the pocket wall at each axial element is obtained by summing the projection of the tangential and radial forces from all of the engaged flutes on the normal direction y_i :

$$F_{yi}(t) = \sum_{j=1}^{N_f} [-\sin \phi_{ji}(t) \cos \phi_{ji}(t)] \begin{bmatrix} F_{tji}(t) \\ F_{rji}(t) \end{bmatrix} g_{ji} \quad (18)$$

where g_{ji} is a unit step function determining whether the flute is engaged with the workpiece ($\phi_{st} < \phi_{ji} < \phi_{ex}$) or not. The entry, ϕ_{st} , and exit, ϕ_{ex} , angles are shown in Fig. 3. The normal deflections alters the entry and exit angles [3], i.e. the cutting forces will vary with the deflection. Since one of the goals of the optimization is to ensure low vibrational amplitudes the effect is neglected in this contribution.

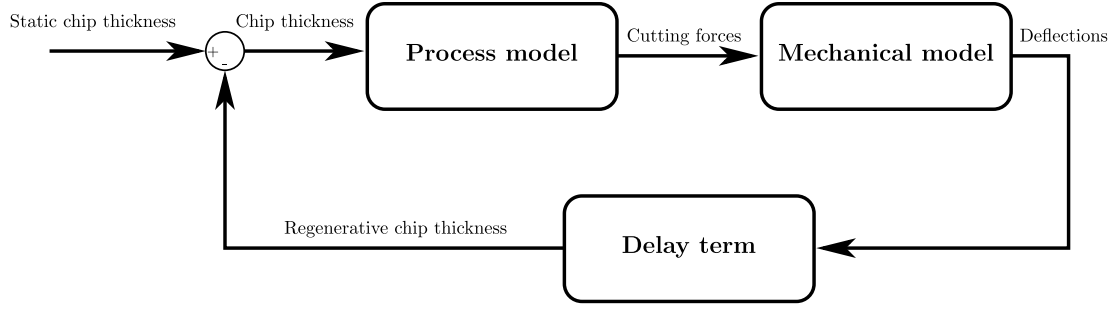


Fig. 4. Closed loop regenerative chatter block diagram.

3.2. Regenerative chatter

The dynamics of chip generation in milling of flexible parts is represented by the closed loop diagram in Fig. 4. The machining process exerts forces on the flexible pocket wall which causes deflection of the structure. The deflection causes the cutting edge to leave a wavy surface, which modulates the thickness of the chip removed by the succeeding flute. According to the diagram in Fig. 4, the overall chip thickness removed at each moment by each flute comprises the static portion, modulated by the deflection of the thin wall, $w_i(t)$, and the waviness left by the preceding tooth at the same location, $w_i(t-T)$, as formulated in Eqn. (16). This mechanism can cause instability of the process vibrations if process parameters (i.e. axial depth of cut a and spindle speed Ω) are selected inappropriately. This phenomena is known as regenerative chatter [16].

If the closed loop system has any poles in the right half of the complex s -plane, the system is unstable. This corresponds to the denominator of the closed loop transfer function having zeros in the right half of the s -plane [20]. Thus, the stability boundary can be determined through the characteristic equation of the closed loop system:

$$[I] - A_0(1 - e^{-sT})[G(s)] = 0 \quad (19)$$

where A_0 is the directional cutting force coefficient which is obtained as follows by following the zero order approximation (ZOA) [16]:

$$A_0 = \frac{N_f \Delta a K_{tc}}{8\pi} [-\sin(2\phi) - 2K_r \phi - K_r \sin(2\phi)]_{\phi_{st}}^{\phi_{ex}} \quad (20)$$

and $K_r = \frac{K_{tc}}{K_{lc}}$ and ϕ_{st} and ϕ_{ex} are start and exit angles of the cut respectively. The stability of the process for a given combination of spindle speed and depth of cut is evaluated through application of the Nyquist stability criterion. All the points in the tool-workpiece engagement zone are considered in the chatter prediction through the entries of the matrix $[G(s)]$ used in Eqn. (19).

In Eqn. (19), A_0 is the average term in Fourier expansion of the time-periodic directional coefficients [21]. Contribution of the neglected higher harmonic components of these time-periodic coefficients to the stability of the system depends on radial immersion and the number of flutes, as discussed in Ref. [22]. The zero order approximation yields accurate stability predictions in most practical machining conditions, but the higher order harmonics may become significant in low radial immersion machining. Discrete time domain methods such as the Semi-Discretization Method (SDM) can be used to include the higher harmonic components [23], but the computation time is significantly larger than for ZOA. For instance, performing ZOA at one combination of spindle speed and depth of cut takes a few seconds, while performing SDM takes a few minutes. Therefore, ZOA will be used in this work and the effect of neglected harmonics will be compensated for by selection of a larger safety margin in the optimization algorithm as explained in Section 4.4.

3.3. Forced response

The periodic cutting forces cause forced vibrations of the thin pocket wall. The surface quality can become poor if the deflection amplitudes are large, and the pocket wall might not be within the tolerance requirements. The steady state response of the structure is solved through Eqn. (12) in the frequency domain (i.e. $s = i\omega$). The deflection vector $\mathbf{w}(i\omega)$ is transformed to time domain $\mathbf{w}(t)$ by performing an inverse Fourier transform. The deflection vector describes out-of-plane deflections of the wall at the center points of the tool discs ($O_1 \dots O_{N_d}$). The force vector utilized $\mathbf{F}(i\omega)$ consists of the Fourier transformation of the forces normal to the thin wall computed through Eqn. (18) using only static chip thickness h_{st} in Eqn. (16).

4. Optimization

The purpose of the optimization is to maximize the material removal rate, MRR , which is a function of both radial depth of cut r , axial depth of cut a , feed per tooth s_t , number of flutes N_f and spindle speed Ω :

$$MRR(r, N_f, a, s_t, \Omega) = r N_f a s_t \Omega \quad (21)$$

In this contribution number of flutes and radial depth of cut are assumed to be predefined, leaving the design variables axial depth of cut, feed per tooth and spindle speed. The design variables are normalized with their maximum limits (a_{max} , s_{tmax} , Ω_{max}) which are governed by the capacity of the endmill and machine tool. The normalized design variables are collected in a vector of design variables $\Gamma = [a_{norm} s_{tnorm} \Omega_{norm}]$.

Consider an arbitrary toolpath discretized into N_p points as shown in Fig. 5. The axial depth of cut is normal to the plane, and the deflection vector for point k (\mathbf{w}_k) consists of deflections for all N_d points in the axial depth (Eqn. (13)). At the cutter location k , the material removal

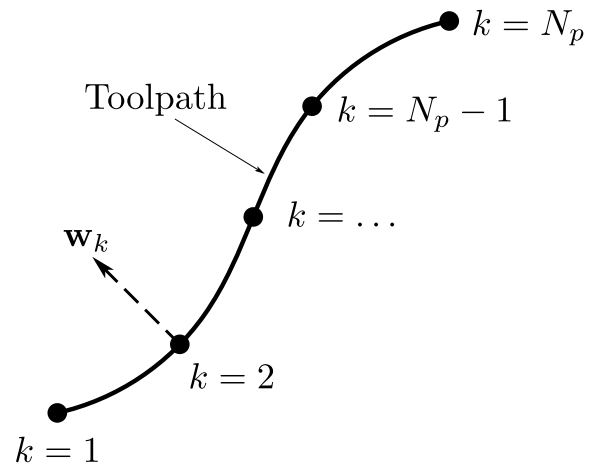


Fig. 5. Arbitrary planar toolpath.

rate optimization problem can be formulated as:

$$\begin{aligned} \text{minimize}_{\Gamma} \quad & f(\Gamma) = \left[\left(1 - \frac{MRR(r, N_f, \Gamma)}{MRR(r, N_f, \Gamma_{max})} \right) \cdot 100 \right]^2 \\ \text{subject to} \quad & \text{real}(\text{roots}(|\mathbf{I}| - A_0(\Gamma)(1 - e^{-sT(\Gamma)})[G_k(s)]|)) < 0 \\ & w_{ki}(\Gamma) \leq w_{max} \quad \text{for } i = 1 \dots N_d \\ & \Gamma_{min} \leq \Gamma \leq \Gamma_{max} \end{aligned} \quad (22)$$

where $MRR(r, N_f, \Gamma_{max})$ is the maximum possible material removal rate for the specific setup and w_{max} is the maximum allowed deflection based on tolerance requirements of the part. Surface Location Error (SLE), where deflections are projected to errors left on the machined surface, can be implemented instead of dynamic deflections [24,25]. However, dynamic deflections provides more conservative cutting parameters, requires less computation when solving the optimization problem and is simpler to assess in real applications. Design variable limits Γ_{min} are above or equal to zero while $\Gamma_{max} = [1 \ 1 \ 1]$ due to the normalization. The machine tool is assumed to have sufficient power and torque capabilities to conduct the machining process as specified. The first constraint enforces a stable process, i.e. the real parts of roots of the characteristic equation (Eqn. (19)) has to be negative to avoid unstable poles. In the stability constraint equation, $[G_k(s)]$ is the transfer function (Eqn. (11)) evaluated at the cutter location k . The transfer function, i.e. the finite strip model, is updated every time a new cutter location k is selected. The second constraint defines that deflections normal to the feed direction cannot exceed the threshold given by w_{max} .

In this paper, the design variables Γ are kept constant throughout one pass around the pocket i.e. axial depth of cut, feedrate and spindle speed are not varied once the tool is engaged with the workpiece. Therefore, the optimization has to comply with the constraint equations for all N_p points along the toolpath without varying the design variables Γ . This leads to a requirement that the constraint equations of Eqn. (22) can not be violated for $k = 1, 2, \dots, N_p - 1, N_p$. When applied to the finite strip model of this paper the points k are selected as the center points of the strips in the horizontal direction ($u=0.5 \Delta u$). The vertical coordinates, v , are chosen to ensure a match with tool discretization i as illustrated in Fig. 2.

4.1. Penalty cost function

No closed-form solutions exist for the stability and deflection constraints for the general system, and it is computationally heavy to obtain them numerically. Furthermore, the constraints have to be computed for all points k along the toolpath, and recomputed whenever the transfer function $[G_k(i\omega)]$ changes due to the variation of the mass and stiffness distribution as material is removed during the machining process.

To ensure fast computation, the two constraints are included in the cost function ($f(\Gamma)$) as penalty terms instead [15]. Thereby, it is not necessary to precompute constraint equations for the entire design space in advance. The reformulated optimization problem is stated in Eqn. (23).

$$\begin{aligned} \text{minimize}_{\Gamma} \quad & f(\Gamma) = \left[\left(1 - \frac{MRR(r, N_f, \Gamma)}{MRR(r, N_f, \Gamma_{max})} P_e(\Gamma) \right) \cdot 100 \right]^2 \\ & P_e(\Gamma) = 1 - \sum_{k=1}^{N_p} (P_{ck}(\Gamma) + P_{dk}(\Gamma)) \\ \text{subject to} \quad & \Gamma_{min} \leq \Gamma \leq \Gamma_{max} \end{aligned} \quad (23)$$

The chatter penalty terms $P_{ck}(\Gamma)$ and deflection penalty terms $P_{dk}(\Gamma)$ are elaborated in Sec. 4.2 and Sec. 4.3, respectively. The reformulation of the constraints to penalty form renders a solution where constraints are not strictly obeyed, hence it is important to select the penalty formulations carefully. The advantage of this method compared to the form of Eqn. (22) is that the convergence rate is higher because the constraints are included in the costfunction thereby directing the optimization routine towards an optimum solution which is in the feasible

range. Cutting parameter (Γ) boundaries are maintained as inequality constraints as in Eqn. (22). The finite strip model is updated every time the costfunction is computed.

4.2. Chatter penalty

The chatter penalty term is designed to take on values between zero and one, and to increase abruptly as the milling process approaches instability. The penalty term for cutter location k is formulated as the following piecewise function:

$$P_{ck}(\Gamma) = \begin{cases} 1 & \text{if unstable} \\ e^{-c_1 s_{mk}(\Gamma)} & \text{if stable} \end{cases} \quad (24)$$

where c_1 is a scaling constant governing how rapidly the penalty function goes towards one, and s_{mk} represents the stability margin of the system. Large c_1 values encourage solutions closer to the chatter constraints, whereas low c_1 values push the optimization routine further below the chatter constraints (i.e. larger safety margin). Thus, the parameter c_1 must be tuned such that the optimization routine provides sufficiently robust solutions while still being capable of entering narrow stability pockets. Initially, given a set of design variables, the system stability is checked using the Nyquist stability criterion [26]. If deemed stable, the stability margin at cutter location k is computed as the minimum distance between the Nyquist curve of the closed loop system (Fig. 4) and origo on the complex plane:

$$s_{mk}(\Gamma) = \min(|\mathbf{I}| - A_0(\Gamma)(1 - e^{-i\omega T(\Gamma)})[G_k(i\omega)]|) \quad (25)$$

Because the defined distance function describes the minimum distance from the Nyquist curve of the system to the origo point in the complex plane, this stability margin considers both gain and phase margin of the closed loop system simultaneously. The system transfer function $[G_k(i\omega)]$, which is computed using the finite strip model, is updated every time the Nyquist curve is recomputed.

4.3. Deflection penalty

The deflection penalty term is also constructed to take on values between zero and one, and to increase abruptly as the dynamic deflections approach the maximum allowable deflection w_{max} . The deflections of all N_d points in the tool-workpiece engagement zone is checked when evaluating the deflection penalty term. The deflection closest to the deflection limit w_{max} is used to compute the deflection penalty. At the k^{th} cutter location, the penalty term is formulated as:

$$P_{dk}(\Gamma) = \begin{cases} 1 & \text{if } \max(|w_{ki}(\Gamma)|) > w_{max} \\ e^{-c_2 \left(1 - \frac{\max(|w_{ki}(\Gamma)|)}{w_{max}} \right)} & \text{if } \max(|w_{ki}(\Gamma)|) \leq w_{max} \end{cases} \quad (26)$$

where $i = 1 \dots N_d$ and c_2 is a scaling constant governing how rapidly the penalty function approaches one. As with the chatter penalty scaling constant c_1 , the deflection penalty constant c_2 governs the trade-off between robustness and optimality. The larger c_2 value, the closer the optimization will go to the deflection constraint boundary. Small values will ensure large safety margins, while the solution might be sub-optimal. The deflections at the cutter location k is computed according to Sec. 3.3.

4.4. Penalty term constants

Selection of penalty term constants c_1 and c_2 is important for tuning of the optimization routine. The constants can be seen as a trade-off between robustness of the solution and optimality of the solution. If large constants are chosen the optimization will select points closer to the constraints i.e. higher MRR, while small constants yields sub-optimal MRR. Selecting parameters close to the constraints can be dangerous because of uncertain parameters and modelling simplifications.

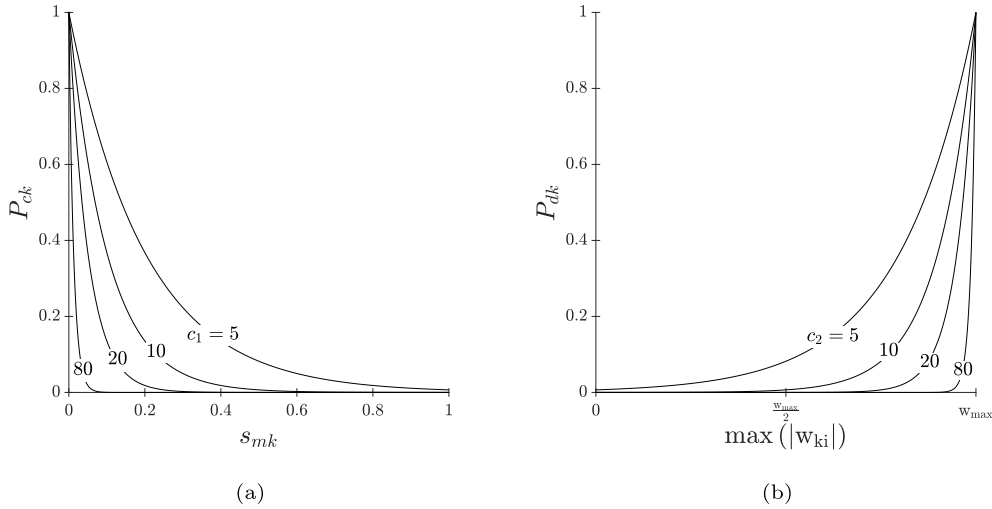


Fig. 6. (a) Chatter penalty term of equation (24) for $0 \leq s_{mk} \leq 1$, (b) deflection penalty term of equation (26) for $0 \leq w_{ki} \leq w_{\max}$ for different values of c constants.

Thus, selection of sufficiently low parameters c_1 and c_2 basically ensures a safety margin which is desirable for simulations of this type. Fig. 6 illustrates how the penalty evolves as process parameters approach the constraint boundaries for different values of c_1 and c_2 respectively. Fig. 6a shows the chatter penalty term of Eqn. (24), and depending on the model certainty selecting parameter c_1 in the range of 20–80 should provide a sound trade-off. Likewise, Fig. 6b shows the deflection penalty term of Eqn. (26), and suggest selection of parameter c_2 in the same range as for parameter c_1 .

An example costfunction is constructed to exemplify how variations of a c constant changes the nature of the penalty cost function. A costfunction of two variables is selected as:

$$f(\Gamma) = e^{-\Gamma_1 \Gamma_2} \quad (27)$$

with variables defined in the ranges $0 \leq \Gamma_1 \leq 1$ and $0 \leq \Gamma_2 \leq 1$. The optimum is located at $\Gamma_1 = \Gamma_2 = 1$ with a costfunctional value of $f(\Gamma) = 0.37$. A synthetic constraint equation is constructed by combination of 4 s order polynomials. The penalty method of Eqn. (22) is implemented to enforce constraints on the cost function. Fig. 7 illustrates how the penalized costfunction varies with the c constant in the exponential penalty term formulation. For $c = 5$ large grey regions exist below the constraint boundary (red dashed line), and an optimization routine will find the optimal solution at approximately $\Gamma_1 = 0.42$ and $\Gamma_2 = 0.30$ yielding a cost functional value of $f(\Gamma) \approx 0.88$. For the case of $c = 80$ the grey regions close to the constraint equation are narrow i.e. the routine can select values close to the constraint. An optimization routine will find the optimal solution at approximately $\Gamma_1 = 1.00$ and $\Gamma_2 = 0.65$ yielding a cost functional value of $f(\Gamma) \approx 0.52$. This example illustrates that with large c constants an optimization routine can find solutions close to the true limit and that lower c constants (e.g. 20) ensure additional safety margin to the constraints.

4.5. Critical point identification

The computation time of the cost function can be reduced by limiting the number of points along the toolpath, N_p , taken into account. In this contribution a critical point identification technique is proposed to automatically identify the most flexible points on the structure, which are then used as the N_p points in the cost function, Eqn. (23).

The proposed method is based on the power mode indicator function [27], which sums the squared of the absolute value of direct- and cross transfer functions at each frequency. For the k^{th} cutter location along the toolpath the power mode indicator function is calculated as:

$$pMIF_k(i\omega) = \sum_{l=1}^{N_d} \sum_{n=1}^{N_d} |G_{k,nl}(i\omega)|^2 \quad (28)$$

where $G_{k,nl}$ is the element on the n^{th} row and l^{th} column of the transfer function $[G_k(i\omega)]$ computed at cutter location k according to Eqn. (11) with $s = i\omega$. The $pMIF$ values for each k along the toolpath are summed over all frequencies of interest to obtain the critical point index, CPI at cutter location k :

$$CPI_k = \sum_{\omega=0}^{\omega_{\max}} pMIF_k(i\omega) \quad (29)$$

where ω_{\max} is the maximum frequency of interest which is determined by the range of the dominant structural modes. When the CPI is computed for all points along the toolpath the most flexible points can be identified as the points with the largest CPI values. The number of points to include in the optimization is a trade-off between computational efficiency and accuracy of the predictions provided by the dynamic models. Thus by truncating points some important part of the dynamics might be left out.

4.6. Optimization method and resampling scheme

The bound optimization problem stated in Eqn. (23) is solved using a gradient based bound optimization algorithm in MATLAB. The algorithm, called *Interior Point Algorithm*, solves the problem iteratively using barrier functions [28]. The true bound minimization problem is reformulated into a series of approximate problems. For the approximate problems the inequality constraints are reformulated into equality constraints. The solution to the approximate problem converges toward the solutions of the original problem as the number of iterations increase. The algorithm does not leave the feasible part of the design space. The gradients are approximated numerically.

The optimization problem is not convex, meaning that multiple local minima exists along with the global minimum. No mathematical conditions which characterize the global optimum exist for such problems [15]. A method for coping with this type of problems is to rerun and resample the problem a large number of times and then accept the solution as the correct solution. A resampling scheme based on the search history of the optimization routine is developed and implemented in this contribution to increase the likelihood of determining the global minimum instead of local minima. The resampling scheme is based on solving the optimization problem (Eqn. (23)) multiple times (N_s) with randomly chosen initial design variables $\Gamma_0 = [\Gamma_{01} \ \Gamma_{02} \ \dots \ \Gamma_{0N_p}]$ where N_p denotes number of design variables, e.g. three in this work. The search history iterations,

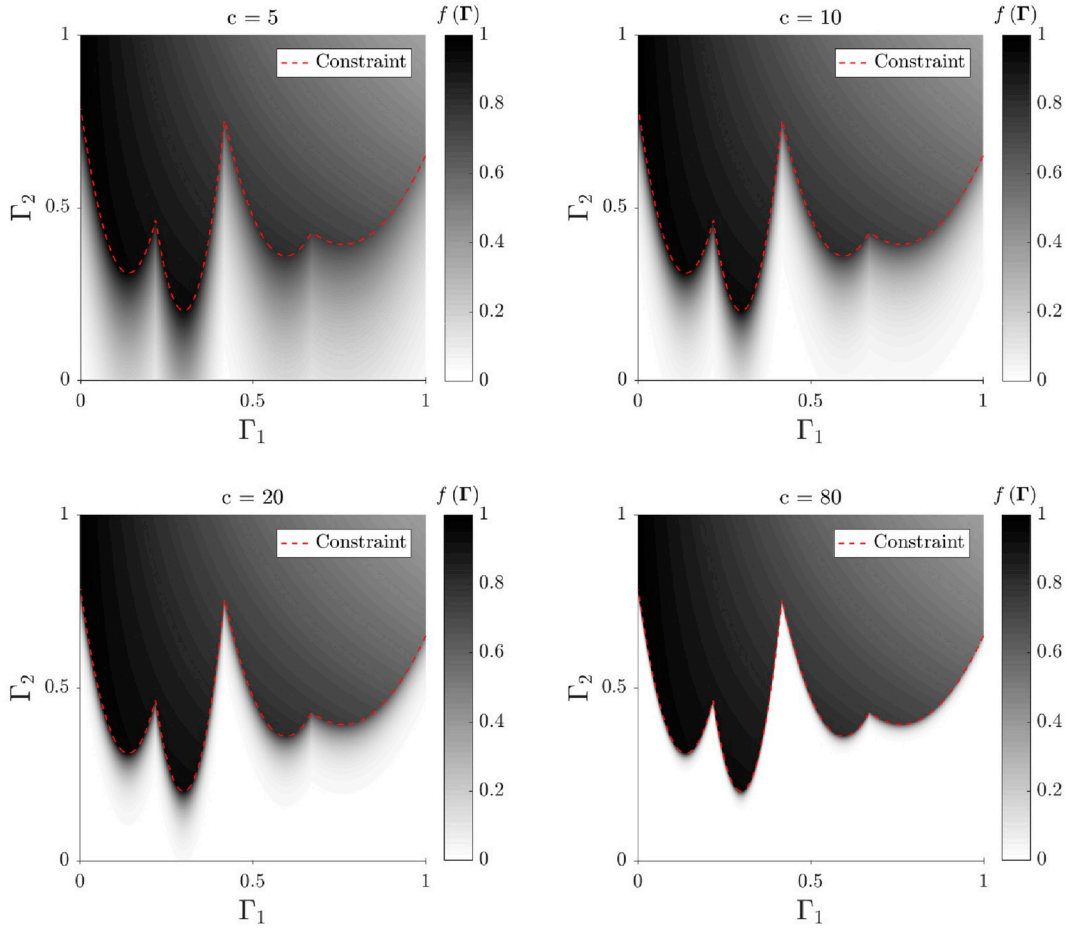


Fig. 7. Costfunction example of equation (27) with penalty from shown constraint function defined by the red dashed line. Penalty is enforced using the method of equation (24) where the penalty constant c is different for the four plots. (For interpretation of the references to colour in this figure legend, the reader is referred to the Web version of this article.)

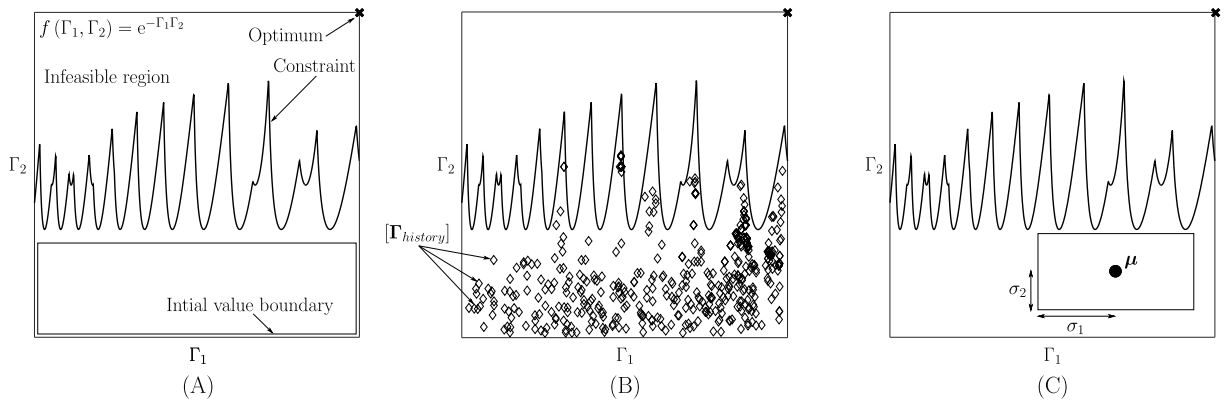


Fig. 8. Resampling strategy. (A) initialization through definition of initial value boundary in the feasible set of solutions. (B) optimization problem is solved multiple times with random initial parameters within initial value boundaries. All search iterations are stored in array $[\Gamma_{history}]$. (C) initial value boundaries are redefined based on mean values and standard deviations of $[\Gamma_{history}]$. Parts (B) and (C) are repeated multiple times.

$[\Gamma_{history}] = [\Gamma_{h1} \ \Gamma_{h2} \ \dots \ \Gamma_{hN_b}]$, is used to redefine the boundaries of the initial guess region N_b times. Fig. 8 illustrates a few steps of the process for the costfunction of Eqn. (27) of two variables Γ_1 and Γ_2 and a complicated stability-lobe-like constraint equation. Initial (A), an initial value boundary which bounds a region of feasible designs is specified. Second (B), the optimization problem is solved N_s times with different initial values which are inside the initial value boundary. All iterations of the N_s optimization algorithm executions are stored in the search history array $[\Gamma_{history}]$. Thus, the length of the search history array (N_h) is

dependent on how many iterations the optimization routine has taken. Third (C), the search history array, $[\Gamma_{history}]$, is utilized to redefine the initial value boundary. The lower and upper boundaries for the design variables, IVB_l and IVB_u , are redefined using the mean and standard deviations of the search history array as:

$$IVB_l = \mu - \sigma \quad (30)$$

$$IVB_u = \mu + \sigma \quad (31)$$

where $\mu = [\mu_1 \ \mu_2 \ \dots \ \mu_{N_b}]^T$ and $\sigma = [\sigma_1 \ \sigma_2 \ \dots \ \sigma_{N_b}]^T$ are the

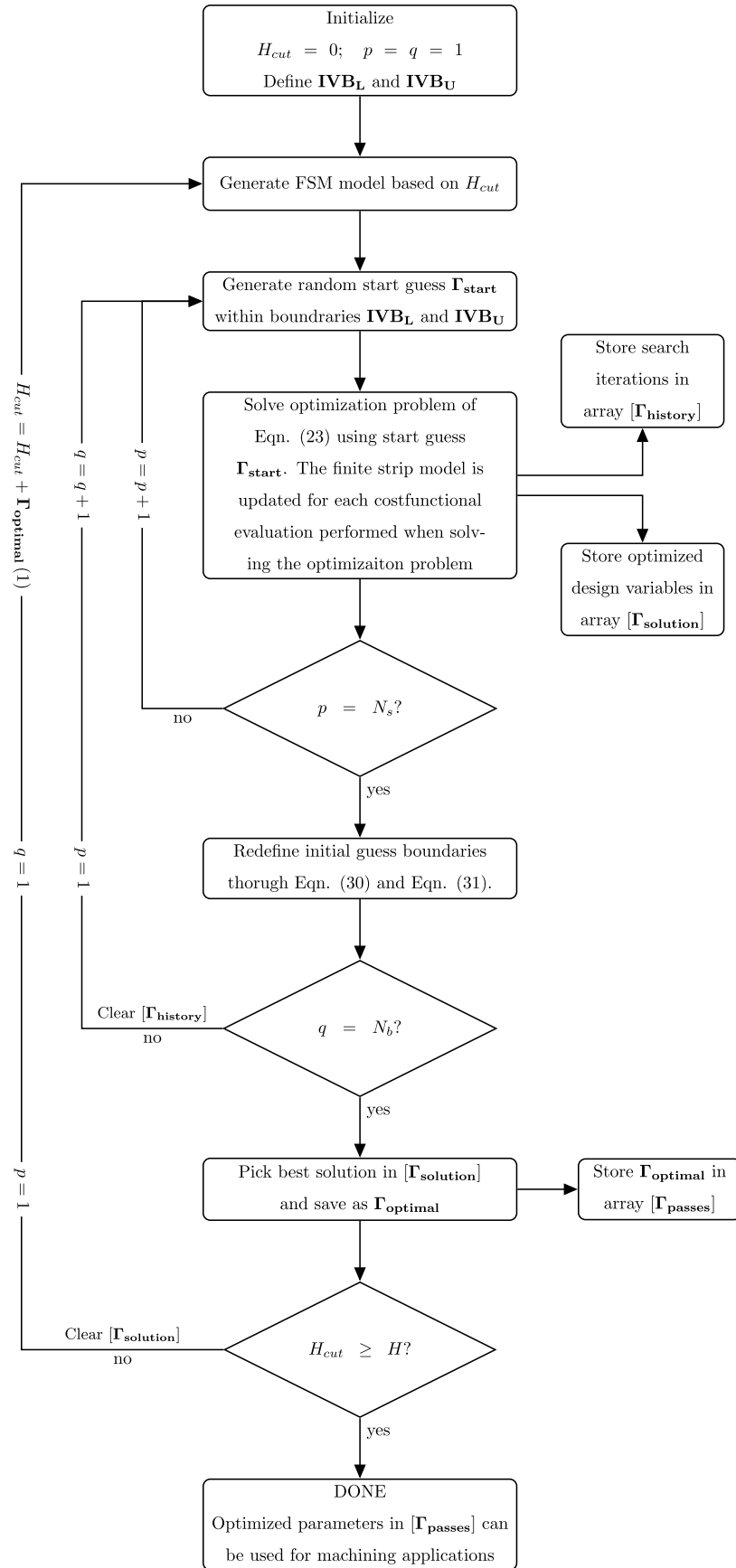


Fig. 9. Optimization scheme flowchart.

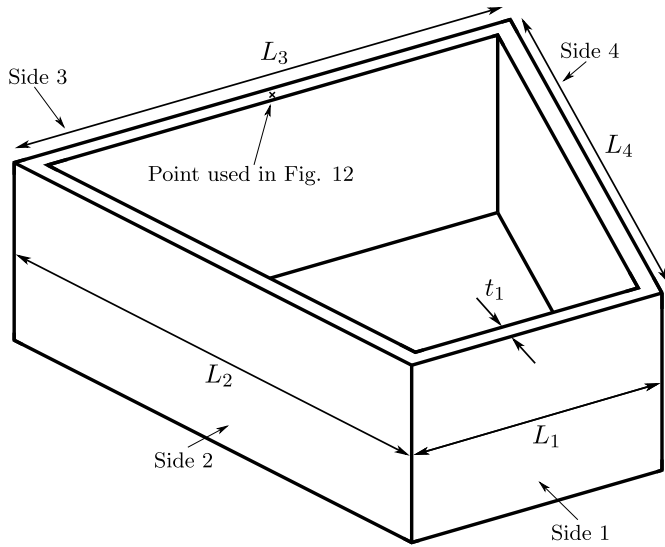


Fig. 10. Pocket geometry case study. The point at the top-center of side 3 is used for numerical validation in Fig. 12 of sec. 6.1.

vectors of mean values and standard deviations for each design variable respectively. The mean value and standard deviation of each design variable, Γ_v where $v = 1 \dots N_v$, are calculated as:

$$\mu_v = \frac{1}{N_h} \sum_{h=1}^{N_h} \Gamma_{hv} \quad (32)$$

$$\sigma_v = \sqrt{\frac{1}{N_h} \sum_{h=1}^{N_h} (\Gamma_{hv} - \mu_v)^2} \quad (33)$$

where N_h is the number of entries in each column of the search history array. Steps (B) and (C) are repeated N_b times. Initial value boundaries are only allowed to shrink. The boundary from the previous step is kept if Eqn. (30) or Eqn. (31) yields expanded boundaries.

4.7. Optimization scheme overview

An overview of the optimization routine is provided in this section through the flowchart shown in Fig. 9. The routine is initialized by defining the total cut height as $H_{cut} = 0$, and as iterations progress the axial depth of cut of the optimal solution ($\Gamma_{optimal}(1)$) is added to H_{cut} . The finite strip model is updated for every evaluation of the costfunction in the problem, and considers the pass-history described by H_{cut} . The optimization routine iterates until the full height of the pocket H is machined. Iterations p can be solved using parallel computing methods.

5. Case study

In this section, a case study is presented to demonstrate the application of the presented modelling and optimization approach to maximize MRR in milling of a sample pocket structure. The sample pocket structure is shown in Fig. 10. The pocket dimensions are side lengths $L_1 = 40$ mm, $L_2 = L_3 = L_4 = 80$ mm, wall thicknesses $t_1 = 3$ mm and pocket height $H = 30$ mm. Side one and three of the pocket are parallel. The maximum out-of-plane deflection allowed during machining is chosen as 0.10 mm. The workpiece is produced from aluminium 7075 with Young's modulus $E = 72$ GPa, Poisson's ratio $\nu = 0.33$ and density $\rho = 2810$ kg/m³. Modal damping is determined using experimental modal analysis with an accelerometer and an impact hammer. The first four modes are found to be dominant, hence relevant to include in the optimization. Their damping ratios are found to be $\zeta = [0.75\% \ 0.72\% \ 0.70\% \ 0.40\%]$. The semi-finishing operation is conducted using a two-flute end mill of diameter $d_{tool} = 16$ mm with

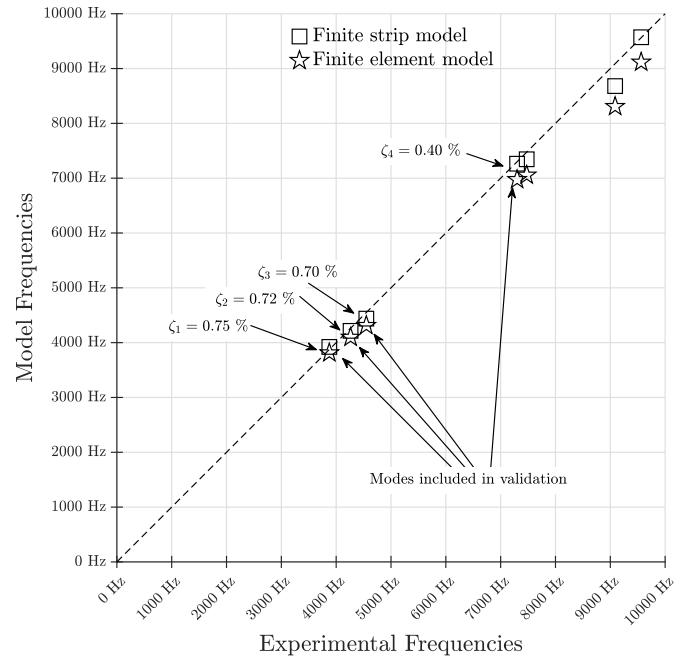


Fig. 11. Comparison of model natural frequencies to experimental frequencies. Modes which are included in numerical and experimental validation are indicated with their respective damping ratios.

helix angle $\beta = 50^\circ$. The maximum axial depth of cut possible with the tool is 30 mm. The axial engagement is discretized using $N_a = 10$ discs. Feedrate limits are selected as minimum $0.05 \frac{\text{mm}}{\text{flute}}$ and maximum $0.25 \frac{\text{mm}}{\text{flute}}$ based on recommendations from the tool manufacturer. The semi-finishing operation conducted reduces the wall thickness from 3 mm to 2 mm in one pass, hence the radial depth of cut is $r = 1$ mm. The machining is conducted on the outside of the pocket wall. Maximum allowable spindle speed is $12000 \frac{\text{rev}}{\text{min}}$. Machining experiments are conducted on a Mazak VARIAXIS i-700 CNC machine tool using downmilling without coolant. The entry and exit angles of the process are $\phi_{st} = 151.05^\circ$ and $\phi_{ex} = 180.00^\circ$. The linear cutting force model of Eqn. (14) is used with cutting force coefficients $K_{fc} = 767$ MPa, $K_{rc} = 255$ MPa, $K_{fe} = 27$ N/mm and $K_{re} = 31$ N/mm obtained through orthogonal to oblique transformation [29] performed in CutPro [30].

5.1. Validation of finite strip model

The discretization parameters for the finite strip model of the pocket are chosen through convergence analysis. Strip width is chosen as $\Delta u = 8$ mm, leading to a total of 35 strips. The number of harmonic terms included in the finite strip model is $m = 6$. The natural frequencies of the finite strip model are compared to experimentally determined frequencies in Fig. 11. The experimental data is obtained using experimental modal analysis. A plate finite element model is established for further validation, and comparison to experimental results are shown in Fig. 11. The finite element model is build in Abaqus CAE, and consists of 568 plate elements of the type S8R which is an eight-node shell element with reduced integration and six degrees of freedom per node. The boundary conditions are identical to the finite strip model boundary conditions i.e. the lower boundary is fixed and the translational degrees of freedom of the pocket corners are locked. Material properties are identical to the finite strip model parameters listed in the beginning of this section. The maximum error of the finite strip model frequencies is 4.7 % and for the plate finite element model the maximum frequency error is 9.4 %. For the experimental work the frequencies are extracted from frequency response function plots, while the results from the two models are obtained through eigenvalue analysis of the undamped systems. The difference in accuracy of the two

models are caused by the differences in assumptions; The finite strip model assumes thin-plate theory where only plate bending is considered, whereas the S8R element in Abaqus assumes thick-plate theory i.e. including membrane effects in the formulation.

6. Numerical validation

This section covers validation of the proposed optimization formulation through numerical examples. The cost function presented in Eqn. (23) is implemented in the examples and results are compared to results obtained using commercial software. Furthermore, the ability of the optimization scheme and the proposed resampling scheme to obey constraints is studied.

6.1. Cost function evaluation

For the pocket structure described in Sec. 5, the cost function defined in Eqn. (23) is evaluated for all points in an equally spaced grid on the spindle speed and depth of cut plane, shown in Fig. 12. The penalty terms used are $c_1 = 75$ and $c_2 = 50$. The feedrate is kept constant at $0.25 \frac{\text{mm}}{\text{flute}}$. The direct frequency response function at the topmost mid-point of side 3 of the pocket in the unmachined configuration, see Fig. 10, is used for evaluation of the cost function. The frequency response function at this point is computed by including the four modes highlighted in Fig. 11 in the frequency response computation in Eqn. (11). The resulting frequency response function was also used in the machining simulation software, CutPro [30], to obtain the corresponding stability lobe diagrams. Fig. 12 shows the resulting cost function and the corresponding stability lobe diagrams; the whiter the region, the lower the cost function value. As shown in this figure, both chatter (grey region) and forced vibration (dark region) boundaries are clearly determined by the cost function. An example of the forced vibration pocket entering a stability pocket is seen at the stability pocket at $\Omega \approx 11800 \frac{\text{rev}}{\text{min}}$. Moreover, the stability boundaries agree very well with the stability lobe diagrams obtained using CutPro. According to the resulting cost function map, chatter is the main limiting constraint for the selected point on the structure. Hence, the optimum machining parameter is located inside one of the stability pockets.

6.2. Optimization iterations

Iteration data from the optimization algorithm is investigated to validate whether the algorithm and resampling strategy efficiently converge to the optimum cutting conditions. Fig. 13 shows the

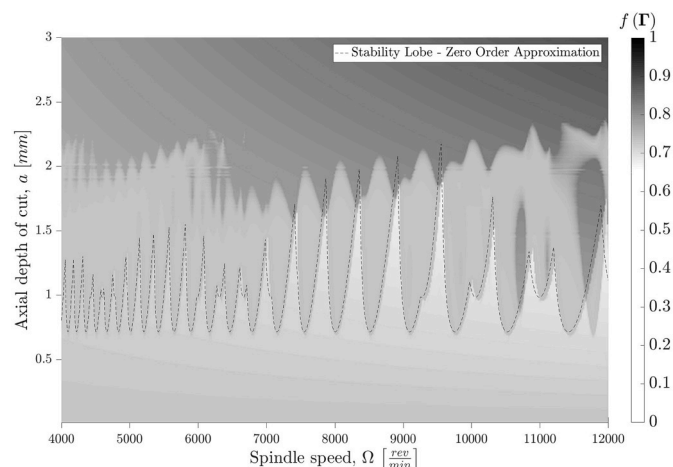


Fig. 12. Cost function for first pass at the center point of side 3 of the case study pocket. The cost function is normalized to a maximum value of 1. The whiter the region the higher material removal rate. Reference stability lobe plotted as dashed line.

iterations of pass number 1 for the pocket structure in this case study. The penalty terms used are $c_1 = 75$ and $c_2 = 50$ and resampling parameters are $N_s = 10$ and $N_b = 3$. The finite strip model is updated for each costfunctional evaluation throughout the computation of the iteration points. The stability boundary plotted is a superposition of boundaries for the five most flexible strips on the pocket determined using Eqn. (29). The stability boundary is determined using CutPro. The deflection boundary is determined through the dynamic model presented in this paper. The method described in Sec. 3.3 is used to determine deflections for a given set of parameters. For a fine grid of spindle speeds, the maximum axial depth of cut is determined which does not cause deflections above w_{max} . The boundary plotted is a worst case combination of boundaries for the five most flexible strips in the unmachined configuration. The same transfer function matrices, $[G(s)]$, are applied for determining both the stability and deflection boundaries. The transfer function matrix is computed for each strip along the toolpath, in the unmachined condition i.e. without accounting for dynamic variations caused by the material removal. It is seen that the stability boundaries are properly negotiated, but a few iterations enter areas of the design space which is constrained by the deflection boundary. The violation might be a false error due to the difference in the frequency response functions used in the optimization and the boundary computation respectively. For the optimization algorithm the penalty boundaries changes for every update of design variables Γ , whereas the boundaries shown in Fig. 13 are based on frequency response functions of the unmachined geometry.

The analysis of this particular optimization solution indicates that the global optimum might not have been found. The stability pocket at approximately $\Omega \approx 8900 \frac{\text{rev}}{\text{min}}$, see Fig. 13 (A), is the best solution found by the optimization algorithm (see Table 1). The peak of the pocket at $\Omega \approx 10300 \frac{\text{rev}}{\text{min}}$, see Fig. 13 (B), yields approximately 30 % higher material removal rate, but since the plotted constraint boundaries does not consider variations of dynamics this lobe might not be a valid solution after all. The varying dynamic response, caused by material removal, changes the natural frequencies of the structure. This could cause the deflection constraint to cancel out the entire stability pocket.

7. Experimental validation

A machining experiment is conducted to verify that the optimized process parameters are in fact valid. The optimization method is executed for the full process of machining the wall thickness from 3 mm to 2 mm for the case study presented in Sec. 5. The optimization routine computation time was approximately 5–6 h, and the resulting cutting parameters for each pass are given in Table 1. It is noteworthy that the depth of cut is larger for the first pass than for pass two and three. This is counter intuitive since the tool-workpiece engagement zone is more flexible for the first pass than pass two and three. The reason can be explained using Fig. 13. At a spindle speed of $\Omega \approx 8900 \frac{\text{rev}}{\text{min}}$ the dominant constraint is stability, and it is possible to perform a deep cut. At a spindle speed of $\Omega \approx 11200 \frac{\text{rev}}{\text{min}}$ the deflection constraint is dominant, which yields a lower allowable depth of cut. Due to the dynamics of the structure changing from pass 1 to pass 2, the stability pocket at $\Omega \approx 8900 \frac{\text{rev}}{\text{min}}$ might have disappeared, thus causing a new optimal solution to exist at $\Omega \approx 11200 \frac{\text{rev}}{\text{min}}$. The feedrates listed in Table 1 are almost identical, but the parameter was free in the optimization routine. The optimization is performed according to Sec. 4, with parameters $c_1 = 75$, $c_2 = 50$, $N_s = 10$ and $N_b = 3$. The parameters are tuned through test runs of parts of the optimization method. This section describes the experimental setup and the results obtained from the experiments.

7.1. Setup

The workpiece is mounted in the CNC machine with the sensors shown in Fig. 14. Cutting forces are measured using a dynamometer, vibrations are measured using an accelerometer and sound is measured

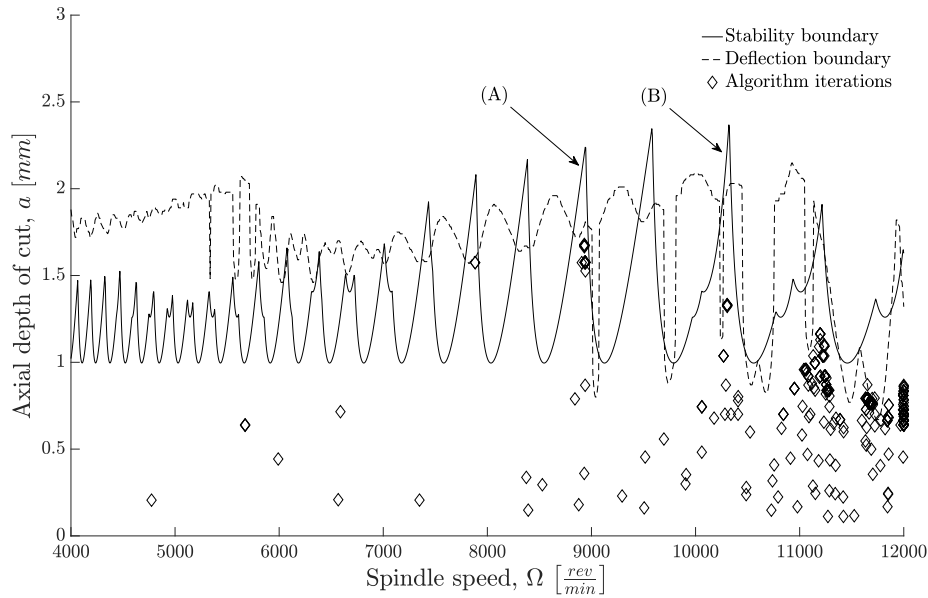


Fig. 13. Optimization scheme iterations and worst case constraint boundaries for pass number 1 of the case study. (A) is the stability pocket which the optimization routine converges to. (B) is the stability pocket with the highest material removal rate.

Table 1
Optimized pocket machining parameters.

Pass	Axial depth of cut	Spindle speed	Feedrate
	[mm]	$\left[\frac{\text{rev}}{\text{min}}\right]$	$\left[\frac{\text{mm}}{\text{flute}}\right]$
1	1.42	8941	0.25
2	1.01	11270	0.25
3	1.06	11245	0.25
4	1.42	11222	0.24
5	1.73	11221	0.25
6	2.50	11198	0.24
7	2.39	11755	0.24
8	5.26	11309	0.24
9	13.21	12000	0.25

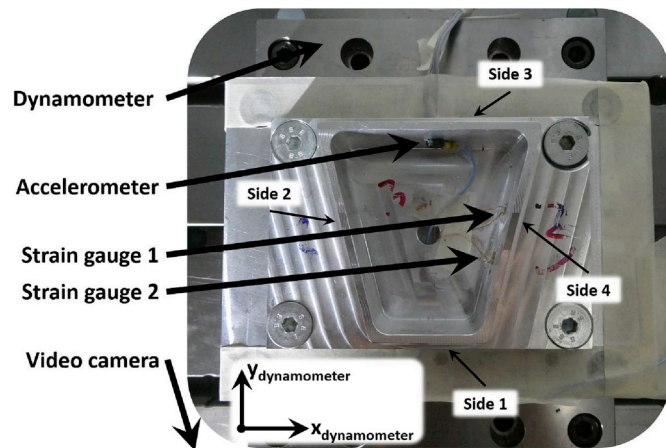


Fig. 14. Picture of experimental setup in cnc machine. The video camera is placed outside the picture.

using a digital video/audio recorder. Deflections are measured indirectly using two strain gauges. The dynamometer is a Kistler 9139AA model, with a sampling rate is 20 kHz. The accelerometer is a PCB 352C23 ceramic shear type, and acceleration is sampled at 10 kHz with an NI-9234 DAQ unit. The accelerometer is attached to the wall using

wax in the center of side 3, as shown in Fig. 14. Two HBM LY41-3/120 linear strain gauges are mounted on side 4. The gauges are mounted in the middle of the wall in the height direction. In the length direction of the wall the gauges are mounted 10 mm from the center in each direction. Strain gauge 1 is the one closest to side 3, and strain gauge 2 is the one closest to side 1, as shown in Fig. 14. Strain is sampled at 10 kHz with an NI-9235 Quarter-Bridge DAQ unit. Sound is extracted from video recordings of the process. The sound is sampled at 48 kHz. All data is recorded and stored on a PC for subsequent analysis.

7.2. Results

The measured signals are assessed separately for each individual pass. The machined surfaces are evaluated after each pass. Simulated cutting forces in the direction normal to the wall are compared to measured forces for all nine passes to verify the accuracy of the force model. The stability of the process is determined through surface quality inspection and frequency domain analysis of the measured sound, cutting force and acceleration signals. The x and y direction forces are combined to obtain the resulting in plane force prior to transforming the signal to the frequency domain. Deflections are evaluated indirectly through comparing measured strains to computed maximum allowable strain. The expected strains at the locations of the strain gauges are computed by assuming that the maximum allowed deflection occurs at the top of the tool-workpiece engagement zone. More details on the computation are given in Sec. 7.2.3. Detailed stability and forced vibration results for pass 1 and pass 9 are presented in this paper. Pass 1 is chosen because the workpiece is most flexible for that pass, and pass 9 because it is the most aggressive cut conducted. All nine passes have been investigated using the same procedure as for pass 1 and 9, and the conclusions are the same for all passes; the process is stable and the deflection limit is not exceeded.

7.2.1. Cutting forces

Forces are measured for each pass in the x-y frame of the dynamometer. The forces have been projected to the normal direction for the four pocket walls, and frequencies beyond the bandwidth of the sensor (2 kHz) are filtered out. Fig. 15 shows the maximum absolute simulated and experimentally measured forces for each pass of the machining process. The forces are simulated using the linear mechanistic force model of Eqn. (18) considering the static part of the chip thickness (h_{st})

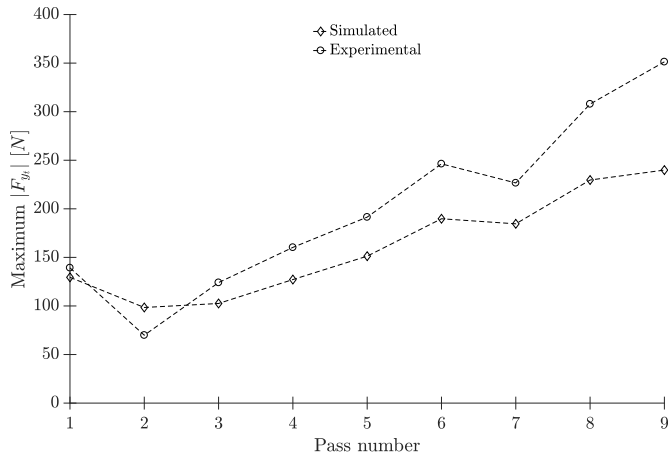
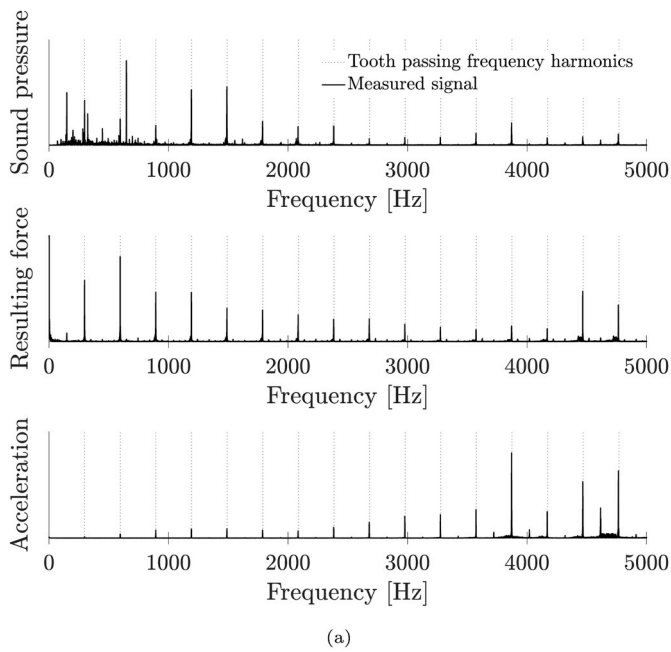
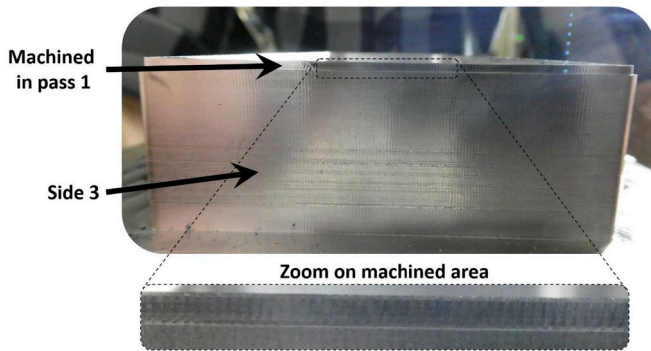


Fig. 15. Maximum absolute simulated and experimental forces for pass one to nine.



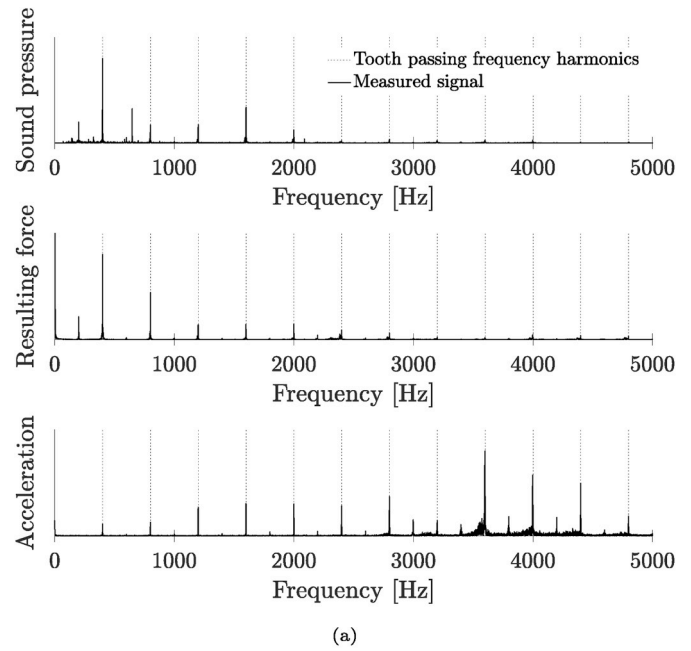
(a)



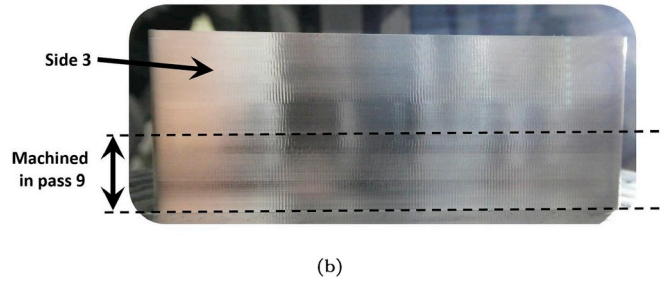
(b)

Fig. 16. (a) FFT of sound, force and vibration signals recorded for pass 1 and (b) side number 3 after machining of pass 1.

only. The measured and simulated forces are in close agreement and show similar tendencies. The general under-estimation of the forces is caused by neglecting the workpiece vibrations in the simulated forces.



(a)



(b)

Fig. 17. (a) FFT of sound, force and vibration signals recorded for pass 9 and (b) side number 3 after machining of pass 9.

7.2.2. Chatter stability

For pass 1, the most flexible pass, the dominant natural frequency is the second natural frequency which occurs at approximately 4200 Hz, see Fig. 11. The FFT of the sound, force and acceleration signals for pass 1 are shown in Fig. 16a where the tooth passing frequency harmonics are indicated by dotted lines. No frequencies around any of the work-piece natural frequencies are dominant for either sound nor force measurements. The acceleration signal shows a clear peak at 3870 Hz, which is resonance of the first natural frequency of the pocket structure. The peak at the dominant second natural frequency (4200 Hz) is not excessively excited. Fig. 16b shows part of the finished surface on side 3 after pass 1. Marks left on the surface are identified as run-out marks, because their distance are two times the feedrate distance (0.50 mm). Sides 1,2 and 4 show the same regular pattern. Based on frequency spectra of measured signals and surface inspections pass 1 is deemed stable.

During pass 9 the chatter frequency changes significantly due to the large change in natural frequencies caused by the mass and stiffness change as material is removed from the structure. Before performing pass 9, the dominant natural frequency is estimated at approximately 4300 Hz using the finite strip model of Sec. 2. After the pass the dominant frequency has shifted to approximately 3400 Hz. The FFT of the sound and force signals for pass 9 are shown in Fig. 17a. Again, no frequencies around the dominant natural frequencies are seen in either sound or force signal. A clear peak is found at 3600 Hz in the acceleration signal, which again is concluded to be resonance caused by the harmonics of the cutting force. Fig. 17b shows side 3 after machining pass 9. Similar to pass 1 (and all of the intermediate passes) the regular

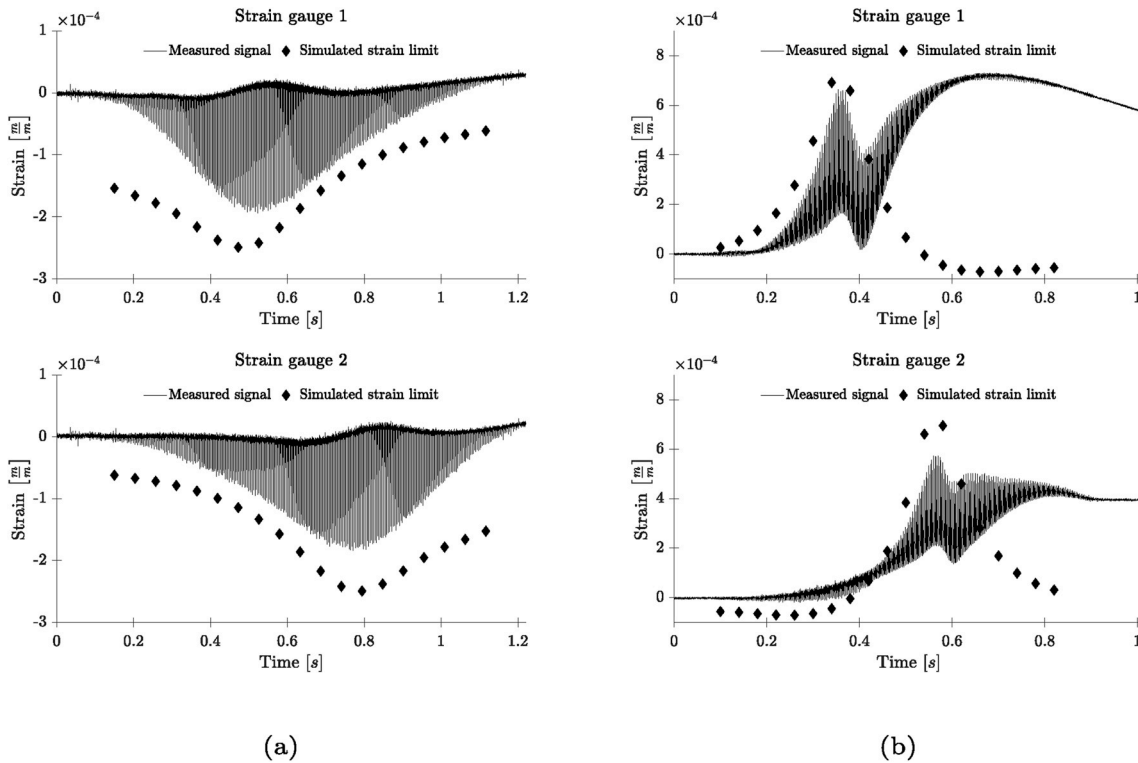


Fig. 18. Measured strain compared to simulated maximum allowable strain for side 4 in (a) pass 1 and (b) pass 9.

surface marks are identified as run-out marks. Sides 1, 2 and 4 show the same surface characteristics. Thus, pass number 9 is deemed stable.

7.2.3. Forced vibrations

Strains are measured for two points on side 4 of the pocket. When the tool is engaged with sides 1, 2 and 3 the measured strains are small and close to the noise level in the signal. Therefore, measured strains are only compared to simulated strains for the period of time where the tool is machining side 4. Strain limits are computed through the finite element model presented in Section 5. The geometry and mesh of the finite element model is redefined for each pass to reflect the impact of the varying wall thickness. A deflection equal to w_{\max} is applied at the current tool point at the top of the workpiece-cutting tool engagement zone (i.e. $i = N_a$), and membrane strains at the two strain gauges are computed for the v coordinate direction (Fig. 1).

Fig. 18a shows comparison of the measured strains to the simulated strain limits for pass 1. For both strain gauge 1 and 2 the measured strains are below the simulated strain limits.

Fig. 18b shows the comparison plot for pass 9. A general trend of the measured strains being below the simulated strains is found. For strain gauge 1 the measured strain climbs beyond the strain limit at around 0.45 s until around 0.70 s where it starts decreasing. The strain decreases towards zero (beyond the plot limits). The zero strain is reached long after the tool is no longer engaged with the workpiece. The behaviour is assessed as being temperature increase at the strain gauge due to the delay before increasing, and the relatively slow decay after the tool has disengaged with the workpiece. The same conclusion applies for strain gauge 2, as well as several of the passes which is not presented directly in this paper.

8. Conclusion

An optimization problem with the objective of maximizing material removal rate constrained by stable vibrations with bounded amplitudes is formulated. The cost function is formulated using penalty terms which penalize the function as chatter and forced vibration constraints

are approached. Penalty terms for multiple cutter locations along the toolpath can be included, and a critical point identification method is proposed to aid selection of important cutter locations. A gradient based optimization routine is applied to solve the optimization problem, and a resampling strategy is implemented to minimize the risk of convergence to a local minimum. The cost function and the optimization resampling strategy are developed in a general manner to ensure applicability to both flexible cutting tools and/or flexible workpieces.

The method is applied to a thin-walled four sided aluminium pocket as a case study for verification and validation. The pocket is modelled using computational efficient finite strip modelling. The duration of the optimization routine for the case study is approximately 5–6 h. Balancing of computational cost against optimality and robustness is possible through e.g. the model discretization, number of critical points considered, number of resampling steps etc. Nonetheless, considering that optimization is performed offline and only one time during process planning stage, 5–6 h of computation time is comparable to the time that is typically spent for process planning in many applications. An example of the topography of the cost function is shown and successfully compared to a zero order stability lobe estimate obtained using a commercial machining simulation software. Iterations from one optimization execution are analysed to clarify whether the optimization routine respects the constraints successfully. In general, the routine obeys the constraints but a few iterations enter the infeasible part of the design space through the optimization iterations. The violation is believed to be a false error since the plotted boundaries are generated without accounting for varying workpiece dynamics whereas the optimization routine updates the finite strip model for every iteration. A crucial part of application of the proposed method is selection of penalty term constants. The constants provides an opportunity to adjust the trade-off between robustness and optimality of the solution i.e. selecting low constants yields large safety margins to the constraints and high constants yields narrow safety margins. Finally, machining experiments are conducted to validate the optimization strategy in a real machining setup. The case study pocket structure is machined in nine passes, determined by the presented optimization setup. All nine passes

are deemed stable and to obey the deflection limits defined based on various signals recorded during machining.

Acknowledgements

This contribution is a product of a six month research stay at Dynamics and Digital Manufacturing research laboratory at University of Victoria and Manufacturing Automation Laboratory at University of British Columbia. Assistance and hospitality of Dr. Keivan Ahmadi, Dr. Yusuf Altintas and their respective research teams is greatly appreciated. Furthermore R&D Technician Jan Jensen from Danish Advanced Manufacturing Research Center have been of great help in conducting the experimental work. The work for this article is a part of the Danish research project InnoMill, contract number 54-2014-3. Funding provided by the Innovation Fund Denmark is greatly acknowledged.

Appendix A. Supplementary data

Supplementary data to this article can be found online at <https://doi.org/10.1016/j.ijmachtools.2019.103430>.

References

- [1] J.K. Rai, P. Xirouchakis, Finite element method based machining simulation environment for analyzing part errors induced during milling of thin-walled components, *Int. J. Mach. Tool Manuf.* 48 (6) (2008) 629–643.
- [2] W. Chen, J. Xue, D. Tang, H. Chen, S. Qu, Deformation prediction and error compensation in multilayer milling processes for thin-walled parts, *Int. J. Mach. Tool Manuf.* 49 (11) (2009) 859–864.
- [3] X. Zhang, C. Xiong, Y. Ding, X. Huang, H. Ding, A synthetical stability method for cutting parameter optimization to assure surface location accuracy in flexible part milling, *Int. J. Adv. Manuf. Technol.* 75 (5–8) (2014) 1131–1147.
- [4] S. Bolsunovskiy, V. Vermel, G. Gubanov, I. Kacharava, A. Kudryashov, Thin-walled part machining process parameters optimization based on finite-element modeling of workpiece vibrations, *Procedia Cirp* 8 (2013) 276–280.
- [5] U. Bravo, O. Altuzarra, L.L. De Lacalle, J. Sánchez, F. Campa, Stability limits of milling considering the flexibility of the workpiece and the machine, *Int. J. Mach. Tool Manuf.* 45 (15) (2005) 1669–1680.
- [6] O. Adetoro, W. Sim, P. Wen, An improved prediction of stability lobes using nonlinear thin wall dynamics, *J. Mater. Process. Technol.* 210 (6–7) (2010) 969–979.
- [7] L. Arnaud, O. Gonzalo, S. Seguy, H. Jauregi, G. Peigné, Simulation of low rigidity part machining applied to thin-walled structures, *Int. J. Adv. Manuf. Technol.* 54 (5–8) (2011) 479–488.
- [8] M. Baumann, P. Eberhard, Interpolation-based parametric model order reduction for material removal in elastic multibody systems, *Multibody Syst. Dyn.* 39 (1–2) (2017) 21–36.
- [9] O. Tuysuz, Modeling of Machining Thin-Walled Aerospace Structures, Ph.D. thesis, University of British Columbia, 2018.
- [10] Y. Yang, W.-H. Zhang, Y.-C. Ma, M. Wan, X.-B. Dang, An efficient decomposition-condensation method for chatter prediction in milling large-scale thin-walled structures, *Mech. Syst. Signal Process.* 121 (2019) 58–76.
- [11] D. Wang, J. Ren, W. Tian, K. Shi, B. Zhang, Predicting the dynamics of thin-walled parts with curved surfaces in milling based on fem and taylor series, *Int. J. Adv. Manuf. Technol.* (2019) 1–16.
- [12] K. Ahmadi, Finite strip modeling of the varying dynamics of thin-walled pocket structures during machining, *Int. J. Adv. Manuf. Technol.* 89 (9–12) (2017) 2691–2699.
- [13] E. Budak, A. Tekeli, Maximizing chatter free material removal rate in milling through optimal selection of axial and radial depth of cut pairs, *CIRP annals* 54 (1) (2005) 353–356.
- [14] X. Zhang, H. Ding, Note on a novel method for machining parameters optimization in a chatter-free milling process, *Int. J. Mach. Tool Manuf.* 72 (2013) 11–15.
- [15] J. Arora, Introduction to Optimum Design, Elsevier, 2004.
- [16] Y. Altintas, Manufacturing Automation: Metal Cutting Mechanics, Machine Tool Vibrations, and CNC Design, Cambridge university press, 2012.
- [17] J. Stefani, K. Ahmadi, O. Tuysuz, Finite strip modeling of the varying dynamics of shell-like structures during machining processes, *J. Manuf. Sci. Eng.* 140 (4) (2018) 041015.
- [18] S.S. Rao, Vibration of Continuous Systems, John Wiley & Sons, 2007.
- [19] A. Brandt, Noise and Vibration Analysis: Signal Analysis and Experimental Procedures, John Wiley & Sons, 2011.
- [20] C.L. Phillips, H.T. Nagle, Digital Control System Analysis and Design, Prentice Hall Press, 2007.
- [21] Y. Altintas, E. Budak, Analytical prediction of stability lobes in milling, *CIRP annals* 44 (1) (1995) 357–362.
- [22] S. Merdol, Y. Altintas, Multi frequency solution of chatter stability for low immersion milling, *J. Manuf. Sci. Eng.* 126 (3) (2004) 459–466.
- [23] T. Insperger, G. Stépán, Semi-discretization method for delayed systems, *Int. J. Numer. Methods Eng.* 55 (5) (2002) 503–518.
- [24] A.K. Kiss, D. Bachrathy, G. Stepan, Cumulative surface location error for milling processes based on tool-tip frequency response function, *Procedia CIRP* 46 (2016) 323–326.
- [25] B.P. Mann, K.A. Young, T.L. Schmitz, D.N. Ditley, Simultaneous stability and surface location error predictions in milling, *J. Manuf. Sci. Eng.* 127 (3) (2005) 446–453.
- [26] M. Eynian, Y. Altintas, Analytical chatter stability of milling with rotating cutter dynamics at process damping speeds, *J. Manuf. Sci. Eng.* 132 (2) (2010) 021012.
- [27] M. Radeş, A comparison of some mode indicator functions, *Mech. Syst. Signal Process.* 8 (4) (1994) 459–474.
- [28] R.H. Byrd, J.C. Gilbert, J. Nocedal, A trust region method based on interior point techniques for nonlinear programming, *Math. Program.* 89 (1) (2000) 149–185.
- [29] E. Budak, Y. Altintas, E. Armarego, Prediction of milling force coefficients from orthogonal cutting data, *J. Manuf. Sci. Eng.* 118 (2) (1996) 216–224.
- [30] M.A. Laboratories, Cutpro machining simulation, <https://www.malinc.com/products/cutpro/>, version 12.0.69.1.